World Scientific
www.worldscientific.com

THE CLASSIC/CLIMB BEAM COMBINER AT THE CHARA ARRAY

T. A. TEN BRUMMELAAR[*,||], J. STURMANN[*], S. T. RIDGWAY[†], L. STURMANN[*],
N. H. TURNER[*], H. A. MCALISTER[‡], C. D. FARRINGTON[*],
U. BECKMANN[§], G. WEIGELT[§] and M. SHURE[¶]

[*]The CHARA Array, Georgia State University
Mount Wilson Observatory, CA 90123, USA

[†]National Optical Astronomy Observatory
P. O. Box 26732, Tucson, AZ 85726-6732

[‡]Center for High Angular Resolution Astronomy
Georgia State University, P. O. Box 3969, Atlanta, GA 30302-3969

[§]Max Planck Institute for Radio Astronomy
Auf dem Hügel 69, Bonn, Germany

[¶]Exelis — Geospatial Systems, 1919 West Cook Road
Fort Wayne, IN 46818

[||]theo@chara-array.org

In the same way that every telescope has multiple instruments and cameras, an interferometric array like the CHARA Array will have numerous beam combiners at the back end. And like the instruments of a single telescope, each of these combiners will be optimized for a particular kind of observation or scientific program. In this paper we describe the CLASSIC and CLIMB beam combiners of the CHARA Array. Both are open air, aperture plane, wide bandwidth single spectral channel instruments optimized for sensitivity. CLASSIC is the original two beam combiner used for the first science at CHARA, and it still has the faintest magnitude limit. CLIMB is a three beam expansion of CLASSIC that can also provide closure phase measurements.

1. Introduction

Georgia State University's Center for High Angular Resolution Astronomy (CHARA) has designed and built an optical/near-IR interferometric array on the grounds of Mount Wilson Observatory. The CHARA Array (ten Brummelaar *et al.*, 2005) consists of six 1 m aperture telescopes arranged in a Y-shaped configuration yielding 15 baselines ranging from 34 to 331 m as well as 10 possible phase closure measurements. This permits resolutions for stellar diameter measurements, conservatively defined in terms of reaching the first null in visibility, of as small as 1.6 and 0.4 m as (milliarcseconds) in the K and V bands, respectively.

More detailed information on the CHARA Array design and instrumentation can be found in the numerous internal technical reports available at CHARA's website.[(a)]

While an interferometric array consists of many complex optical systems, for example numerous telescopes (Sturmann *et al.*, 2010), active and adaptive optics (ten Brummelaar *et al.*, 2012) beam transport, delay lines, beam switching, longitudinal dispersion correction (Berger *et al.*, 2003), and so on, the final observable, the visibility amplitude and phase, must be measured by putting the beams from several telescopes together and detecting interference fringes in a beam combiner.

[||]Corresponding author.

[a]http://www.chara.gsu.edu/CHARA/techreport.html

In this paper we will describe the first, and what is still at this time the most scientifically productive, beam combiner constructed for the CHARA Array called CLASSIC and its expansion into a three way beam combiner known as CLIMB (CLassic Interferometry with Multiple Baselines). Both CLASSIC and CLIMB use open air optics to combine the beams in the aperture plane and employ moving mirrors to scan through the fringes in delay. We will begin in Sec. 2 with a description of the instrument itself, followed by a short discussion of the theory in Sec. 3, and a description of the data analysis methods in Sec. 4. We finish with a brief discussion of planned upgrades for the instrument in Sec. 5.

2. The Instrument

Both CLASSIC and CLIMB are relatively simple open air aperture plane beam combiners[b] consisting of beam splitters and dispersion compensation plates. It is for this reason that the original two beam version was dubbed CLASSIC. CLIMB is a three way system such that one output of CLASSIC is combined with a third telescope creating two outputs that contain three beams and therefore also a closure phase signal.

2.1. *CLASSIC — A two way aperture plane beam combiner*

The optical layout of CLASSIC is given in Fig. 1. The beams from two telescopes enter from the right. Here, we assume that these beams are adjusted to
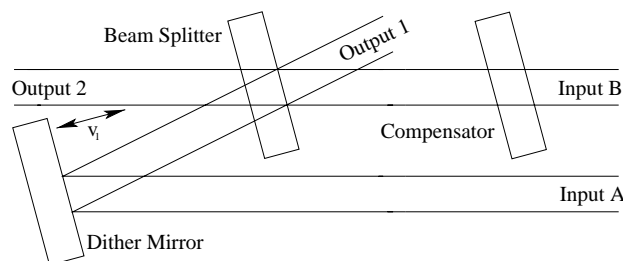

Fig. 1. Schematic of the optical layout of the CLASSIC beam combiner.

---

[b]Note that we are avoiding the term "Michelson beam combiner", a terminology that is, in our opinion, very misleading — Michelson's stellar interferometer created fringes in the image plane, not the aperture plane, and was in fact a "Fizeau beam combiner" — another term we shall avoid using.

the correct phase, ignoring for the moment atmospherically induced piston motion, by the delay line system. One beam, input beam A, is modulated in path-length by what we call a dither mirror. In this way the system can scan through the fringes, something that is known as temporal modulation.

CLASSIC is very similar to many other beam combiners, such as those used at the IRMA (Dyck *et al.*, 1993), COAST (Davis *et al.*, 1999), IOTA (Dyck *et al.*, 1995a), and SUSI (Davis *et al.*, 1999) interferometers. Indeed, the first incarnation of CLASSIC used the same optics and detectors as both the IRMA and IOTA systems. Other interferometers have used similar optical designs, but instead of scanning through the entire packet they scan through only a small number of fringes, often only one, in order to lock onto the fringe phase. Examples of these types of beam combiner are the Mark III (Shao *et al.*, 1988), PTI (Colavita *et al.*, 1999), Keck I (Colavita *et al.*, 1998), PRIMA (Sahlmann *et al.*, 2009), and CHAMP (Berger *et al.*, 2006b) beam combiners. A full description of the so-called "ABCD" method of phase locking used by these types of beam combiners can be found in Colavita (1999).

Let us be clear about the distinction here. In phase locking systems one attempts to lock onto a small part of the fringe phase and track on a single fringe, or small part of a fringe. This allows coherent integration of the fringe data. While CLASSIC is capable of phase locking it is rarely used. Instead it is more common to track to the center of the fringe envelope, a technique known as group delay tracking. While this does not allow coherent integration of the fringe data it is possible to group delay track on stars many magnitudes fainter, and the main objective of the CLASSIC and CLIMB beam combiners is to achieve the best possible magnitude limit. The faintest targets observed to date with CLASSIC have been magnitude 9.3 in the K′ band and magnitude 9.7 in the H band. These limitss were achieved in very good seeing conditions; however, it is routine to observe objects of magnitude 8.5 in both bands.

The dither mirror is driven by a piezo-electric stage with a strain gage acting as a feedback device. The motion of the dither mirror and the read out of the camera are synchronized such that the camera is reading at a steady rate during the linear phase of the dither mirror motion. Furthermore, the velocity of the dither mirror is chosen

to produce fringes at a specified frequency matched to the camera read out rate. We have found that five samples per fringe produces the best data, in the sense that it can be well calibrated, but in fast seeing it is possible to go to as few as three samples per fringe. We have found that more than five samples per fringe does not improve the data quality.

2.2. *CLIMB — CLassic interferometry with multiple baselines*

CLIMB is an extension of CLASSIC to three beams, thus the name CLassic Interferometry with Multiple Baselines. The optical layout of CLIMB is given in Fig. 2. Here, one of the output beams of the CLASSIC layout is combined with a third beam. Note that this means, even in a perfect world, while each output will have the same total amount of light, they will not have the same amount of light from each input. As we shall see in Sec. 3 this can be dealt with fairly easily.

There are two complete CLIMB optical systems in the CHARA Array, each serving three beams in order to match the six telescopes. The two systems can be run in parallel or individually. Since only one detector is used for both systems, if run in parallel they must use the same detector read out rate. A picture and schematic of the complete CLASSIC/CLIMB optical system is given in Fig. 3.

In the CLIMB system that serves beams 4, 5 and 6 it is possible to remove the second (left most) beam splitter and turn it into the CLASSIC two beam combiner. In this way it is possible to operate with either a single or two CLIMB beam combiners, a CLIMB and a CLASSIC beam combiner or just a CLASSIC beam combiner. Like all beam combiners in the CHARA Array, any beams not being used are available for a separate science program with another beam combiner.

The two dither mirrors in the CLIMB system are identical to the one used in CLASSIC. They are also synchronized to the read out of the detector system, although in this case dither mirror 1 moves
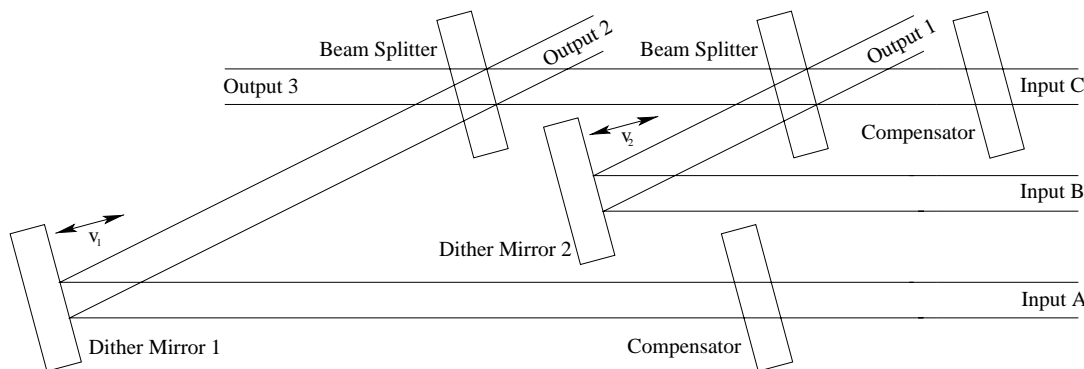

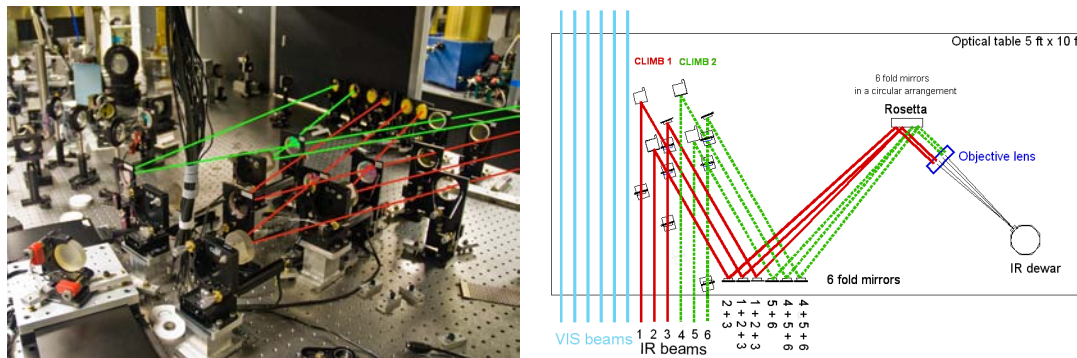Fig. 2.   Schematic of the optical layout of the CLIMB beam combiner.

Fig. 3.   Layout of the CLASSIC/CLIMB optics with optical paths drawn. The picture on the left shows the second CLIMB system in its CLASSIC configuration. The diagram on the right shows both beam combiners in the CLIMB configuration along with the output optics that feed the beams into the detector.

at half the speed, in the opposite direction, and for half the distance as dither mirror 2. In this way the fringes between beams A and C are at some specified frequency, say f_0, the fringes between beams B and C are at $2f_0$, and the fringes between beams A and B are at $3f_0$. The fringes of the highest frequency, those between beams one and two, will normally have five samples per fringe, while those of the other beam pairs will be ten samples per fringe for beams B and C, and fifteen samples per fringe for beams A and C. This can, during times of poor seeing, be reduced to three, six and nine samples per fringe respectively.

Note that if one blocks input beam A and adds the output beams 2 and 3 together one has a system almost identical to CLASSIC, with the only difference being double the read out noise on one side of the beam splitter. It is also possible to block either input beam B or C and use output beams 2 and 3 to form a CLASSIC-like system for the other two pairs of beams. This is referred to as "two beam mode" and is often used for searching for fringes during observing as described in Sec. 2.8. It is also used for collecting so-called separate fringe packet data on binary stars. This will be described in more detail in Sec. 4.3.

2.3. *Beam management and alignment*

The combined output of the two CLIMB systems is six beams: three parallel to the input beams, and three at 30° to this direction. Each of these six beams must be focused onto a different pixel of the detector system, and this requires a fairly specialized optical feed system. The current setup uses two steering mirrors, the minimum, for each beam combiner output. The first set of steering mirrors is arranged in a row (See Fig. 2) using the same custom-designed flex mounts we use in many places in the beam combination laboratory. The mounting of the second set of steering mirrors, called the Rosetta, is designed specially for CLIMB to optimize the layout of the input beams and minimize the diameter of the first optical element. Pictures of the Rosetta and the first objective lens are shown in Fig. 4.

2.4. *The detector — The near infra-red observer (NIRO)*

The detector currently used is a Rockwell 256×256 HgCdTe PICNIC array with $40\,\mu$m pixels. This chip is capable of QE's better than 60% in the wavelength range of 1 to 2.3 μm. NIRO was based on the camera used at the IOTA interferometer (Millan-Gabet *et al.*, 1999; Pedretti *et al.*, 2004) and was built with the kind assistance of Drs. Wes Traub and Rafael Millan-Gabet, at that time of the Harvard-Smithsonian Center for Astrophysics.

The PICNIC array is sensitive to light at wavelengths of 0.8 to 2.5 μm and each of its four 128×128 quadrants has its own output amplifier. Since we need only six pixels, NIRO has been wired to read out only one quadrant, and we align this quadrant such that the pixels of interest are as close as possible to the corner connected to the output amplifier. Data acquisition is controlled by a digital I/O board in a PC with a custom-built interface box
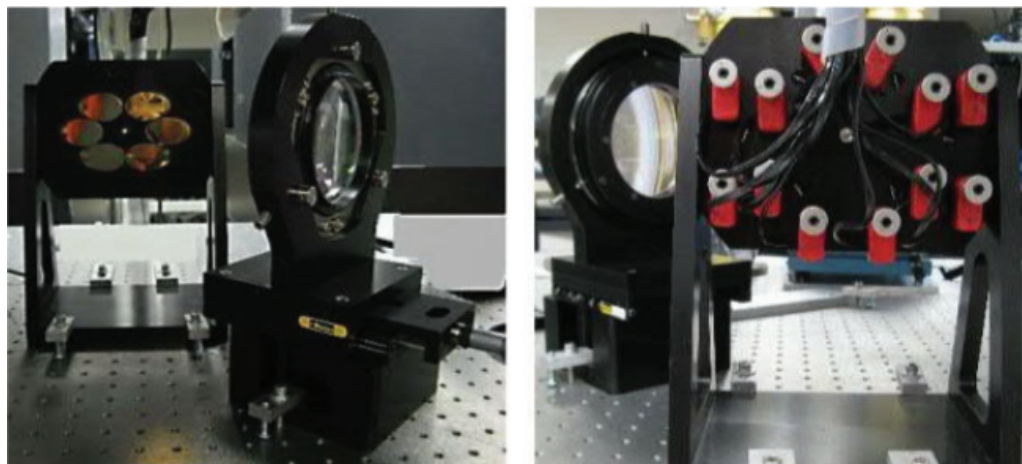

Fig. 4. Two pictures from opposite sides of the mount for the second set of steering mirrors, known as the Rosetta, and the first objective of the IR camera optics are shown here. Each mirror has actuators to allow changes in alignment as described in Secs. 2.5 and 2.7.

containing a clock driver board that provides the DC bias levels for the array and an analog-to-digital converter (ADC) board. The array's analog output signal is buffered by a low noise pre-amplifier with a gain of 20 which is then connected to the ADC board. This amplifier is situated on the inside of the dewar lid and operates at room temperature. The ADC is 16-bit and is capable of 100 kilo-samples per second.

The PICNIC array is mounted in an Infrared Laboratories HDL-5 dewar modified for use with liquid nitrogen in both cryogen cans. The vacuum in the dewar is maintained to better than 10^{-6} Torr by a combination of molecular sieves and an ion pump, resulting in a dewar hold-time of about 24 hr. The vacuum window of the dewar is made of fused silica.

2.4.1. NIRO read out modes

There are three modes of operation for NIRO. The first reads out a rectangular area of the quadrant, which may in fact be the entire quadrant. This mode is used for optical alignment as described in Sec. 2.7. In the second mode, the two, three, or six pixels of interest are read continuously and the data is sent to the control system in real time. Sending the data in this manner imposes a small delay in reading out each sample of the array, but is essential in the fringe scanning process described in Sec. 2.8. We call this mode of operation continuous mode. In the third mode the detector reads out the pixels of interest a pre-determined number of times and sends the data to the control system only when the scan is complete. This mode does not suffer from the delay imposed by sending the data to the control system in real time, and is used in the data acquisition mode described in Sec. 2.9. We call this mode of operation scanning mode. Since the detector sampling and dither mirror motion are required to be synchronized during data acquisition, the PC that controls NIRO is also responsible for sending the control voltages to the dither mirrors.

In order to achieve the best possible magnitude limit, when using CLASSIC it is also possible to use a 2×2 pixel area for each of the two outputs. While this introduces more read-noise, and will require a re-alignment of the optics as described in Sec. 2.7, it can increase the amount of light reaching the output. The choice between single pixel read out and 2×2 pixel read out is highly seeing and object

dependent and choosing between the two must be done on a case by case basis.

There are also two different methods of sampling used by NIRO, referred to as destructive and non-destructive samples. In destructive samples the data consist of a long, or sometimes continuous, stream of RESET-READ-READ sequences. Here the value of each sample is the difference between the two reads. Since there is a reset of the area of interest of the chip before each sample, this method is not prone to saturation. Furthermore it can be done continuously and for an arbitrary amount of time. It is for these reasons that this mode is most often used while scanning for fringes and collecting data on brighter objects. The disadvantage of this method is that each reset imposes a small amount of nonthermal noise created by dumping the charge of the previous sample. On very faint objects it is not possible to use destructive reads because the reset noise totally overwhelms the photon count.

In a non-destructive sample, also sometimes called in the literature an "up the ramp" sample, there is a single reset at the beginning of the sequence followed by a large number of reads. Each sample is then the difference between two consecutive reads. The primary advantage of using non-destructive sampling is that, except for the first few samples, there is no reset noise. The primary disadvantage is that the reset at the beginning of the ramp up dissipates the charge of all the samples in the scan so the resulting reset noise is much larger and lasts for a much longer time than it does for the destructive reads. For this reason we impose a delay of 20 milli-seconds after the reset before starting the sample ramp. Another disadvantage of non-destructive sampling is that the pixels can saturate before the scan is complete, and so this mode can only be used on faint stars.

The duration of each sample is determined by how long it takes to "read" each of the pixels. Like all devices of this type it is possible to average multiple ADC measurements and reduce the read out noise. We refer to this as multiple reads. It is also possible to read all pixels of interest multiple times and make an average of these with similar affect. We refer to this procedure as multiple loops. By a combination of multiple loops and multiple reads it is possible to control the duration of each sample. Initially we believed that using multiple loops ensured that the relative phase of the signal in each pixel was better preserved than using only multiple reads, but in practice we have found that this is not in

fact the case.[c] Furthermore, we have found that our read out electronics produces more noise if we use multiple loops than if we use multiple reads. We therefore use only multiple reads to determine the sample rate of NIRO. The default camera read out rates of NIRO are 125, 250, 500, 750 and 1000 Hz, with 500 and 750 being used most often.

Finally, we note that in non-destructive sampling only one "read" is required for each sample, and that read is in fact multiple reads. It is thus possible to read each pixel more than twice as many times per sample in non-destructive mode than it is in destructive mode and it therefore can have lower read out noise. We therefore use non-destructive mode whenever possible.

2.4.2. *Pixel size on the sky*

Before designing the input optics for NIRO, it was necessary to know the optimum angular extent of the $40\,\mu$m pixel when projected on the sky. Of course, there is no single optimum and one must reach a compromise between signal to noise ratio across a range of seeing conditions and observing wavelengths. It is also possible to use this arrangement as a spatial filter for the output beams of CLASSIC/CLIMB. To determine the optimum size a simple simulation was devised to try and analyze the effect of various pixel sizes on raw visibility, visibility stability, throughput, and signal to noise ratio.

Using the existing CHARA atmospheric modeling code (ten Brummelaar, 1995, 1996) a total of fifteen atmospherically distorted wavefront simulations were created with r_0 ranging from 1 to 15 cm, where the r_0 value is for a wavelength of $0.5\,\mu$m. In K' band this represents a range for r_0 of approximately 5 to 75 cm.

Since we are mostly interested in spatial filtering, and spatial filters have no effect on piston, we set the first Zernike term to zero. Changes in piston will reduce the visibility amplitude, but on average will result in a fractional reduction in visibility and this will not change the outcome of these simulations. Residual tip/tilt will result in an increase in scintillation, as well as a reduction in visibility, but will also, on average, cause a fractional change in the final visibility. We have therefore ignored these two effects in these simulations and assumed that

the fringe tracking and fast-tracking servos remove the majority of piston and tip/tilt. As these simulations are done in terms of Zernike coefficients, the delay line and tip/tilt system were modeled by simply setting the first three coefficients to zero.

Each simulation consisted of a sequence of 2500 atmospherically deformed wave-fronts for each of two telescopes calculated in a grid of 65×65 pixels with a time step of 0.01 s between each frame. Each frame is Fourier transformed to obtain an image plane which is then masked using a square mask to simulate the light hitting a pixel of the detector. Finally, the correlation or visibility is calculated for a single wavelength using the four phase algorithm as described in Tango & Twiss (1980). Figure 5 shows an example of the output of this simulation.

Note that since these simulations use a single wavelength, and perfect fringe tracking and tip/tilt servos, the raw visibilities produced are bound to be higher than we would expect in a real system. However, as even with these simplifying assumptions the models took many days to run, we will assume that they nevertheless represent a realistic model of the process of spatial filtering.

Our primary interest is in sensitivity, and therefore it is the signal to noise ratio that is most important. Figure 6 shows plots for signal to noise for a camera with no read noise (NV^2) and one for a noisy detector (NV).

The NV case continues to rise as the size of the spatial filter is increased, while the NV^2 case shows a clear maximum at around $2\lambda/D$. This result is slightly different from the one derived by Keen *et al.* (2001) who find maximum signal to noise at a diameter of $2.4\lambda/D$, the size of the Airy spot. However, their simulation used a round pin hole, rather than the square pixel used in this study. A square spatial filter has a larger area than a round hole by a factor of $4.0/\pi$ which is very close to the ratio of $(2.4/2.0)^2$, so to first order we can say that our two simulations agree very well.

These simulations show that in order to maximize sensitivity we should use a spatial filter of size $2\lambda/D$. Finally we need to consider that there are three primary wavebands used in NIRO and that the size of the spatial filter scales with λ. Furthermore, the seeing scales as $\lambda^{-\frac{6}{5}}$, so the r_0 values in J band will be about two times smaller than in K band. We chose a spatial filter size optimized for the longer wavebands, which are used more often.

---

[c]See for example the last few slides of http://www.chara.gsu.edu/CHARA/Papers/Atlanta2/tenBrummelaar1.pdf.
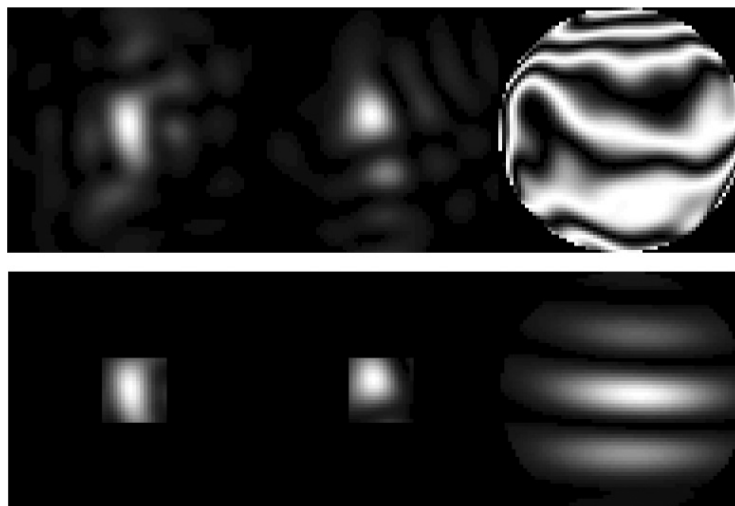
Fig. 5. Two example frames from the simulation, both for $r_0 = 3$ cm. The top plot shows the two image planes and the resulting fringe pattern without a spatial filter, and the bottom plot shows the same frame with a spatial filter of size $2\lambda/D$. In both cases a differential tilt has been imposed on the fringe pattern for display purposes only. Note that, in order to best demonstrate the effect of spatial filtering, the data shown here are for a single frame that was chosen on the basis that it had a greater than average improvement in visibility amplitude and therefore has better seeing than the average.
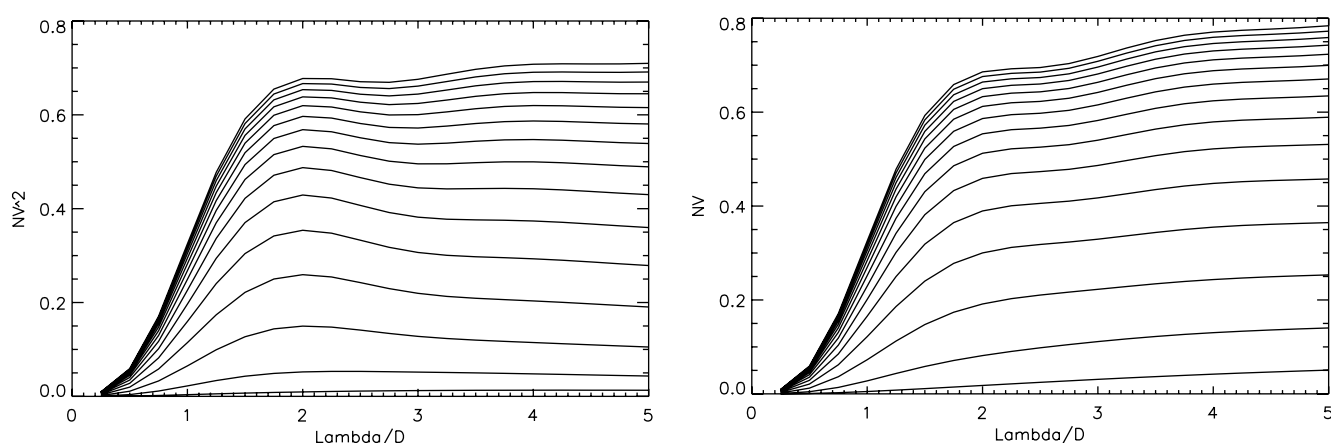

Fig. 6. Final signal to noise ratio for a range of r_0 values from 1 to 15 cm (top to bottom). The X axis shows the size of the spatial filter in terms of the size of the Airy disk, while the Y axis shows the signal to noise ratio of the visibility measurement. The plot on the left shows the signal to noise ratio for a noiseless detector (NV^2), while the plot on the right shows the signal to noise ratio for a noisy detector (NV).

Using the mean wavelength between the H and K′ bands of 1.90 μm, a spatial filter of $2\lambda/D$ represents an angular size of 0.78 arcseconds on the sky. The beam magnification between the telescopes and the laboratory is approximately 53 and so this represents some 42 arcsec in the beam combiner.

2.4.3. NIRO optics

Imaging requirements and constraints, set mainly by the dimensions of the existing dewar, called for custom optics and mounts. Optimax Systems Inc.

manufactured the lenses, and custom mounts were designed and fabricated in-house.

The input to the camera optics is a circular array of six 19 mm diameter collimated beams. The first piece of the camera optics, a 100 mm diameter lens, is outside of the dewar. This objective is mounted on a translation stage equipped with a manual micrometer actuator. Its focal plane lies inside of the dewar near the window. The objective lens can be seen in Fig. 4. The objective is a custom-made air spaced doublet; the substrate of the first element is Suprasil, the second element is CaF_2. The
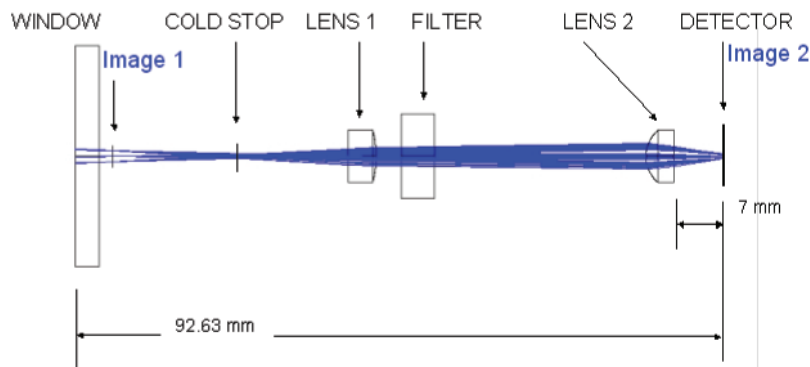
Fig. 7.   Schematic of the light path inside the cold dewar.

first element is anti-reflection coated while, due to the risks associated with coating a CaF$_2$ substrate, the second one is left un-coated.

The rest of the optical elements are inside the dewar. The schematic of the optical path in the dewar is shown in Fig. 7. A cold stop, 0.8 mm in diameter, is placed where the footprint of the six beams is the smallest. This placement of the cold stop minimizes the thermal background while also accommodating the varying pupil image position of the array. There are two plano convex relay lenses, custom-made out of Suprasil. Both have a diameter of 7.5 mm, and both are broadband anti-reflection coated.

Spectral filters mounted in a filter wheel can be moved into the optical path in between the relay lenses where the beams are nearly collimated. The characteristics of the filters, measured at 77 K, are given in Table 1.

2.5.   Laboratory alignment

A visible alignment laser is used throughout the array. This laser marks the beam paths from the internal sources out to each telescope and back to each beam combiner. The initial alignment of CLIMB 1 and CLIMB 2 to NIRO was done at the time of installation, and there is only one target to which CLIMB input beams have to be

adjusted daily. This is enough to see the starlight on the detector and final adjustments can be made using the on-sky alignment procedure described in Sec. 2.7.

Although daily routine alignments are only necessary to the first fiducial at the CLIMB setup, occasionally the whole system needs a tune-up. We use the visible laser and a target, which fits over the large objective shown in Fig. 4 and shows the correct circular pattern for the six beams. Since the cold stop in the dewar is visible through the vacuum window it provides a final target for the laser beams coming from each output of the two beam combiners. This ensures that at least some light passes through the cold stop and we then rely on the on-sky alignment procedure.

2.6.   Focus

Focusing of the camera optics was done using an internal white light source and by adjusting the position of the L2 lens, the one closest to the array inside the dewar. Another focus adjustment is to change the position of the objective outside the dewar along the z-axis. The optimization was done iteratively until the most light was focused onto the designated pixels.

During the initial alignment the focus of the camera optics were optimized in H band, but by design K, or J bands are well focused too. The calculated RMS spot diameters are shown in Table 2. The table shows that if the focus was optimized in H band, the RMS spot diameter is well within the pixel in the other bands too. Ultimately, the seeing, rather than focusing will set the limit of the number of photons in a pixel during observation. The focus of the camera optics has proved to be extremely stable and has not needed adjustment for some years.

Table 1.   Filter characteristics at 77 K.

Band	Center (nm)	FWHM (nm)
J	1286	278
H	1673	285
K$'$	2133	349
K continuum	2089.4	23.5
Bracket-γ	2163.8	21.6

Table 2. Calculated image sizes (μm) in J, H, K bands on the 40 μm detector pixels.

Band center μm	Focused in H band	Focused in each band
J 1.286	22.54	20.50
H 1.673	20.48	20.48
K 2.133	24.28	20.76

2.7. On-sky alignment

While every effort is made to align the optics of CLIMB/CLASSIC before observations begin, it is still necessary to check the alignment on the sky periodically throughout the night. The primary cause of misalignment is differential atmospheric refraction between the visible light used for tip/tilt detection and the near-infrared light used in the beam combiner. Furthermore, since we use Alt/Az telescopes, the images in both the tip/tilt system and the beam combiner are slowly rotating. Small differences in pixel gains in the tip/tilt detector can also cause changes in beam position in the beam combiner. It is therefore necessary to check the alignment of the beam combiner whenever large changes in telescope position have occurred. Note that this on-sky alignment is only performed after a calibrated bracket of observations has been completed.

The on-sky alignment of both CLASSIC and CLIMB has two main goals:

(a) To ensure that each output beam is well centered on the correct pixel of the detector.
(b) To ensure that the beam splitters are aligned to the plane of intersection of the input beams.

It is the first of these criteria that is most severely affected by differential refraction between the tip/tilt and science wavelengths, and alignment of the beam splitter itself is rarely required more than a few times during the night. Furthermore, like many things in a system of this kind, on-sky alignment is very dependent on the seeing and can be quite difficult during times of poor seeing. On-sky alignment must be done on a relatively bright object, normally of 6th magnitude or brighter. Ideally this should be the science target, but a nearby bright star can be used if the science target is too faint.

The on-sky alignment of CLASSIC is a three step process:

(1) With the shutter for input beam A closed, move the Rosetta mirror for output 2 to center the light on the correct pixel on NIRO. This satisfies criteria (a) for output beam 2.
(2) With the shutter for input beam A open and the shutter for input beam B closed, move the beam splitter until output beam 2 is correctly aligned on the same pixel on NIRO. This satisfies criteria (b).
(3) With both shutters open align the Rosetta mirror for output 1 to center the light on the correct pixel on NIRO. This satisfies criteria (a) for output 1.

The on-sky alignment for CLIMB is very similar, but has a few more steps:

(1) With only the input beam C shutter open, align the output 3 Rosetta mirror to center the light on the correct pixel (Criteria (a)).
(2) With only the input beam B shutter open, align the output 1 Rosetta mirror to center the light on the correct pixel (Criteria (a)).
(3) With only the input beam A shutter open, align the output 2 Rosetta mirror to center the light on the correct pixel (Criteria (a)).
(4) With only the input beam C shutter open, align the first (rightmost in Fig. 2) beam splitter to center the light on the output 1 pixel (Criteria (b)).
(5) With only the input beam C shutter open, align the second (leftmost in Fig. 2) beam splitter to center the light on the output 2 pixel (Criteria (b)).

For both CLASSIC and CLIMB, once this alignment procedure has been completed the whole area of interest of the chip can be displayed with all shutters open as a final check that most of the light is falling onto the correct pixels.

2.8. Fringe acquisition

The CHARA Array optical chain has numerous moving parts and long propagation paths, and so despite a good baseline solution the fringes do not always appear at the delay offsets predicted by the astrometric model of the array. For this reason, CLASSIC and CLIMB have a fringe scanning mode. In the case of CLIMB, we search for fringes on two

beams at a time in a manner identical to that of CLASSIC.

Fringe scanning begins by moving the dither mirror to its central position and putting NIRO into the continuous mode described in Sec. 2.4.1 using destructive reads. One of the delay carts is then moved at a constant velocity relative to the astrometric model position so that it will produce fringes at the desired frequency. The system then calculates the difference between the two outputs and displays a bandpass filtered version looking for a high signal to noise event, or indeed fringes visible to the naked eye, at the correct frequency.

The fringe signal to noise ratio is calculated by integrating the power spectrum around the expected fringe frequency

$$P_{\mathrm{fringe}} = \int_{f_0 - \Delta f/2}^{f_0 + \Delta f/2} \mathrm{PS}(f) df, \qquad (1)$$

and the noise in a part of frequency space where we do not expect to see fringes

$$P_{\mathrm{noise}} = \int_{f_0 + 1.5\Delta f}^{f_0 + 2.5\Delta f} \mathrm{PS}(f) df, \qquad (2)$$

and then forming the ratio

$$\mathrm{SNR} = \frac{P_{\mathrm{fringe}} - P_{\mathrm{noise}}}{P_{\mathrm{noise}}}. \qquad (3)$$

The default is that a SNR ≥ 1 represents a fringe detection; however, the operator can override this as well as change the minimum SNR. Since the samples are time tagged, it is possible to calculate the delay line offset at the time the fringes were found. We then switch to data acquisition mode and start collecting data.

If the Array configuration has not changed the fringes are rarely more than a few hundred microns away from the predicted position. If the configuration has been changed the fringe offset may change by many millimeters. For a sample rate of 500 Hz, the default fringe frequency is 100 Hz, so the delay offset velocity for K′ band is approximately 200 μm per second and it normally does not take very long to find the correct fringe offset. There are, of course, times when the SNR is too low to see fringes in a single pass of the delay lines. In these cases one can either search for fringes on a nearby bright star, or go straight to data acquisition mode

and move the delay line offset in small steps until the fringes are acquired.

2.9. *Data acquisition*

Once the correct fringe offset(s) have been found the dither mirror(s) are set to move at the correct rates and amplitudes and NIRO is put into the scanning mode described in Sec. 2.4.1 in either destructive or non-destructive read out mode depending on the brightness of the target. If the fringes do not appear, the delay line carts are moved small distances, normally one third of the dither mirror motion amplitude, until the fringes are found. At this point the data collection sequence begins.

During the data sequence, if the fringe SNR is above a given threshold, normally 1.0, the system marks the scan as containing fringes, and if the fringes are not well centered a correction is sent to the relevant delay line cart. The data sequence is preceded by a shutter sequence in order to collect scans with all shutters closed, and then with each of the shutters open. This is done in order to measure the background and how much light is being received from each telescope in each pixel. This is followed by a predetermined number of scans with all shutters open, by default 200, followed by the same number of scans with the delay line carts moved several centimeters away from the fringe offset. By default the system will attempt to obtain the required number of scans with a SNR above the threshold, followed by the same number of scans away from the fringes; however all scans are saved in the final data file. Once a data acquisition sequence is completed the final offset is saved as a starting point for the next acquisition sequence on this object.

On the very faintest targets the operator can choose to view a time averaged fringe power spectrum, so that while the fringes are not visible in single scans they can be detected as a small peak at the correct frequency in the power spectrum. Unfortunately, since the power spectrum contains no phase information, this scheme does not allow closing of the servo between the beam combiner and the delay lines. Nevertheless, since the required offsets and hour angle for each successful data sequence are recorded, it is normally possible to predict the required offset and rely on open loop tracking using only the astrometric model. If the fringes do not appear they can be re-acquired with the use of small adjustments of delay offset.

3. Theory

Here we give a general nomenclature of an arbitrary N-way beam combiner that uses temporal encoding like CLIMB. We assume that N input beams are combined in some arbitrary way that includes temporal fringe modulation and all beams are, to some extent at least, present in the output beam being considered. We do not require any particular number of outputs as each output beam can be considered in isolation as an independent N-way combiner.

3.1. *The generalized fringe equation*

The output of such an N-way beam combiner can be written as

$$N(\sigma_0, \Delta\sigma) = 1 + \sum_{i=1}^{N-1} \sum_{j=i+1}^{N} T_{ij} V_{ij} \,\text{sinc}[\pi\Delta\sigma v_{ij} t]$$
$$\times \cos[2\pi\sigma_0 v_{ij} t + (\phi_i - \phi_j) + \Phi ij], \quad (4)$$

where we are using the transfer function

$$T_{ij} = \frac{2\sqrt{I_i I_j}}{\sum_{i=1}^{N} I_i}, \quad (5)$$

and I_i is the intensity reaching the output of the beam combiner from input i, V_{ij} is the complex visibility amplitude on baseline ij, $\Delta\sigma$ is the width of the optical filter being used in terms of wave-number $\sigma = \frac{1}{\lambda}$, v_{ij} is the group velocity of the fringes on baseline ij, t is the time, σ_0 is the central wave-number of the optical filter, ϕ_i is the atmospherically introduced phase error of the light from telescope i and Φ_{ij} is the phase part of the complex visibility. In this analysis we have assumed that the optical filter is square, or a "top hat" function, whose Fourier transform is a sinc function. Of course, this works in general — that is, the fringe envelope is the Fourier transform of the filter function.

Equation (4), and indeed our method of obtaining visibility amplitudes, is a generalization of that presented by Benson *et al.* (1995), and further expanded in ten Brummelaar *et al.* (2005).

3.2. *Application of the fringe equation to CLASSIC*

For a two beam combiner like CLASSIC the transfer function in Eq. (5) reduces to

$$T_{AB} = \frac{2\sqrt{I_A I_B}}{I_A + I_B}, \quad (6)$$

which is of course the same as the transfer function given in Benson *et al.* (1995) except that we now use A and B for the two input beams instead of 1 and 2 as this helps to remove some confusion between the input and output beams. For perfect optics and alignment this transfer function will be 1. There is of course a π phase difference between the two outputs and we can therefore write the fringe equation for output i of CLASSIC as

$$N_i(\sigma_0, \Delta\sigma) = 1 + (-1)^i T_{iAB} V_{AB} \,\text{sinc}[\pi\Delta\sigma vt]$$
$$\times \cos[2\pi\sigma_0 vt + \Phi_{AB}], \quad (7)$$

where we include an extra subscript for the transfer function T_{iAB} to acknowledge the fact that, due to imperfections and misalignment in the optics, the two output pixels will not necessarily have the same amount of light from each input beam and may therefore have different transfer functions.

3.3. *Application of the fringe equation to CLIMB*

As we did for CLASSIC, for CLIMB we also need to include an extra subscript to the transfer function to indicate which output we are using, so for output i and input beams j and k we write

$$T_{ijk} = \frac{2\sqrt{I_{ij} I_{ik}}}{I_{iA} + I_{iB} + I_{iC}}. \quad (8)$$

If we assume perfect optics, the transfer functions for the three output pixels for each beam pair, or baseline, are given in Table 3.

Now, in order to ensure that each baseline fringe pattern has a unique fringe frequency, the dither mirror velocities are set such that

$$v_1 = v, \quad \text{and} \quad v_2 = -2v, \quad (9)$$

where $v = f_0 \lambda_0 / 2.0$, f_0 is the desired lowest fringe frequency and λ_0 is center of the optical band. In order to keep things clear, we have not explicitly included the fact that the beam angle of reflection is 15° and have written these equations as

Table 3. CLIMB transfer functions for perfect optics.

Output	T_{AB}	T_{BC}	T_{CA}
1	0	1	0
2	$\frac{1}{\sqrt{2}}$	$\frac{1}{2}$	$\frac{1}{\sqrt{2}}$
3	$\frac{1}{\sqrt{2}}$	$\frac{1}{2}$	$\frac{1}{\sqrt{2}}$

Table 4. CLIMB phases for perfect optics. Note that beam A does not reach output 1 and so no phase is given.

Output	ϕ_A	ϕ_B	ϕ_C
1	—	0	π
2	0	π	π
3	0	0	0

if the reflection was 0°. Furthermore, note that the mirrors move in opposite directions and that the range of motion of the second dither mirror is half that of the first. The result is that

$$v_{AB} = 3v, \quad v_{BC} = -2v, \quad \text{and} \quad v_{CA} = -v. \tag{10}$$

The sign of v_{CA} is negative because when we come to measure closure phase we need to have a closed triangle and $v_{CA} = -v_{AC}$.

The last thing we need is the phase change for each beam on each output, which are set out in Table 4.

We can then write the three outputs of the CLIMB beam combiner as

$$N_1(\sigma_0, \Delta\sigma) = 1 - T_{1BC}V_{BC} \operatorname{sinc}[2\pi\Delta\sigma vt]$$
$$\times \cos[4\pi\sigma_0 vt - \Phi_{BC}] \tag{11}$$

$$N_2(\sigma_0, \Delta\sigma) = 1 - T_{2AB}V_{AB} \operatorname{sinc}[3\pi\Delta\sigma vt]$$
$$\times \cos[6\pi\sigma_0 vt + \Phi_{AB}] + T_{2BC}V_{BC}$$
$$\times \operatorname{sinc}[2\pi\Delta\sigma vt] \cos[4\pi\sigma_0 vt$$
$$- \Phi_{BC}] - T_{2CA}V_{CA} \operatorname{sinc}[\pi\Delta\sigma vt]$$
$$\times \cos[2\pi\sigma_0 vt - \Phi_{CA}] \tag{12}$$

$$N_3(\sigma_0, \Delta\sigma) = 1 + T_{3AB}V_{AB} \operatorname{sinc}[3\pi\Delta\sigma vt]$$
$$\times \cos[6\pi\sigma_0 vt + \Phi_{AB}] + T_{3BC}V_{BC}$$
$$\times \operatorname{sinc}[2\pi\Delta\sigma vt] \cos[4\pi\sigma_0 vt - \Phi_{BC}]$$
$$+ T_{3CA}V_{CA} \operatorname{sinc}[\pi\Delta\sigma vt]$$
$$\times \cos[2\pi\sigma_0 vt - \Phi_{CA}]. \tag{13}$$

Note that Eqs. (7), (11), (12), and (13) do not explicitly include phase noise due to the atmosphere. We need to also keep in mind that the visibility amplitude will vary due to atmospheric seeing.

4. Data Analysis

With this formulation of the outputs of the two beam combiners it is possible to establish methods to estimate the visibility amplitude and phase for each baseline. We consider each of these separately.

4.1. *Extracting visibility amplitude from the data*

For both CLASSIC and CLIMB we find the square of the visibility amplitude using the power spectrum method described in Benson *et al.* (1995) and calculate the unbiased visibility amplitude using the method described in ten Brummelaar *et al.* (2005). We shall not discuss this further here except to say that the noise power for both CLASSIC and CLIMB is estimated from the off-fringe scans collected at the end of the data sequence. This noise power spectrum is then subtracted from the power spectrum of the scans containing the fringes before we perform the integration.

Implementing the amplitude estimator for CLIMB is very similar to CLASSIC, except now we have three input and output beams as well as three baselines to deal with and the procedure is a little different for each baseline. For each of the three outputs we write the un-normalized signals

$$F_{i,\text{unnorm}}(t) = N_i(\sigma_0, \Delta\sigma) - B_i, \tag{14}$$

where B_i is background as measured during the initial shutter sequence. We then obtain the normalized signal by dividing by the mean

$$F_i(t) = F_{i,\text{unnorm}}(t)/\overline{F_{i,\text{unnorm}}(t)}. \tag{15}$$

Having done this for each of the three output beams 1, 2 and 3 we are ready to form the normalized fringe signal for each baseline

$$f_{AB,\text{norm}}(t) = (F_2(t)/T_{2AB} - F_3(t)/T_{3AB})/2$$
$$= V_{AB} \operatorname{sinc}[\pi\Delta\sigma v_{AB}t]$$
$$\times \cos[2\pi\sigma_0 v_{AB}t + \Phi_{AB}] + O_{BC/CA}(t) \tag{16}$$

$$f_{BC,\text{norm}}(t) = (F_1(t)/T_{1BC} + (F_2(t)$$
$$+ F_3(t))/(T_{2BC} + T_{3AB}))/2$$
$$= V_{BC} \operatorname{sinc}[\pi\Delta\sigma v_{BC}t]$$
$$\times \cos[2\pi\sigma_0 v_{BC}t + \Phi_{BC}] + O_{AB/CA}(t) \tag{17}$$

$$f_{CA,\text{norm}}(t) = (F_2(t)/T_{2CA} - F_3(t)/T_{3CA})/2$$
$$= V_{CA} \operatorname{sinc}[\pi\Delta\sigma v_{CA}t]$$
$$\times \cos[2\pi\sigma_0 v_{CA}t + \Phi_{CA}] + O_{AB/BC}(t) \tag{18}$$

where we have added terms of the form $O_{BC/CA}$ to show that the $F_{AB}(t)$ and $f_{CA}(t)$ signals actually can include fringes from other baselines, but at different frequencies. If we restrict the integration limits when we calculate the total power S_{ij} for each baseline we can separate out the fringes of interest in each case, and since we know the central frequency of each fringe this is not too difficult unless the seeing causes the power in the different fringe signals to overlap.

As for CLASSIC the noise power is estimated from the off-fringe scans at the end of the data sequence and is subtracted from the fringe signals to obtain the fringe power spectra. In the case of the signal $f_{BC}(t)$, if all goes well, only the BC fringes will be present, while in the other two outputs we should see only fringes from the AB and CA baselines. In practice there is often a small amount of leakage from the other fringes, signals due to optical misalignment and imperfections in the optical coatings, and so we must carefully choose our integration ranges to avoid cross talk between baselines.

4.2. *Extracting closure phase from the data*

One important, and perhaps most difficult, part of measuring closure phase is ensuring that the signs on all the various parts, and on the final closure phase itself, are correct. In order to correctly obtain closure, the three frequencies used in Fourier space must add to zero. In other words, one must form the triple product of the complex amplitude at the two lowest frequencies and the conjugate of the complex amplitude at the highest frequency. In the case of CLIMB, we must also be very careful about the signs of the various phases as the mirrors are moving in opposite directions.

First, of course, we must obtain a measurement of the phase of the fringes on the three baselines represented in the instrument. Since we know the sample rate of the detector and the fringe frequencies are set to two and three times the lowest fringe frequency, it is relatively easy to choose a segment that contains only one cycle of the lowest frequency fringe, two of the next, and three of the highest frequency. The default is to have 5 samples across the highest frequency fringe, and so this segment would be 15 samples in length. An example of real, albeit very high signal to noise, data is given in the left plot of Fig. 8.

The Fourier transform of this segment will contain, in the first four bins, the DC, one cycle, two cycles, and three cycles per segment complex amplitudes, that is the DC component and the complex amplitudes of fringes we are interested in. Note how almost all the power is contained in the first three frequency bins. We can then extract the amplitude and phase of the three fringe patterns $F(f_{AC})$, $F(f_{CB})$, and $F(f_{AB})$. It is at this point that we need to be careful about the sign of the phases. The CA fringes are reversed due to the geometry of the beam combiner, while the BC are reversed due to the motion of the dither mirrors. We therefore use the triple product,

$$A_{ABC} = F(f_{AB}) \times F^*(f_{BC}) \times F^*(f_{AC}), \quad (19)$$

as our estimator for the closure phase. One final wrinkle is to take into account the fact that the dither mirrors move both forward and backwards on alternate scans and so, given our definition of Φ_{ij} being positive when the phase of i is ahead of the phase of j, we need to take the conjugate of the entire triple product A^*_{ABC} on each alternate scan. In this way, it is possible to obtain a triple product for each segment in each fringe scan, as shown in Fig. 9.
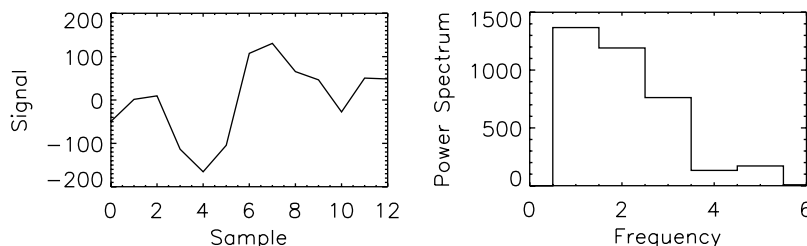

Fig. 8.   Example of extracting the closure phase signal from a single segment. The plot on the left shows the raw signal in output pixel B of a single high SNR segment. The plot on the right shows the power spectrum of this segment. Note that almost all the power is in the first three non-zero frequency bins corresponding to the fringes with one cycle per segment (CA), two cycles per segment (BC) and three cycles per segment (AB).
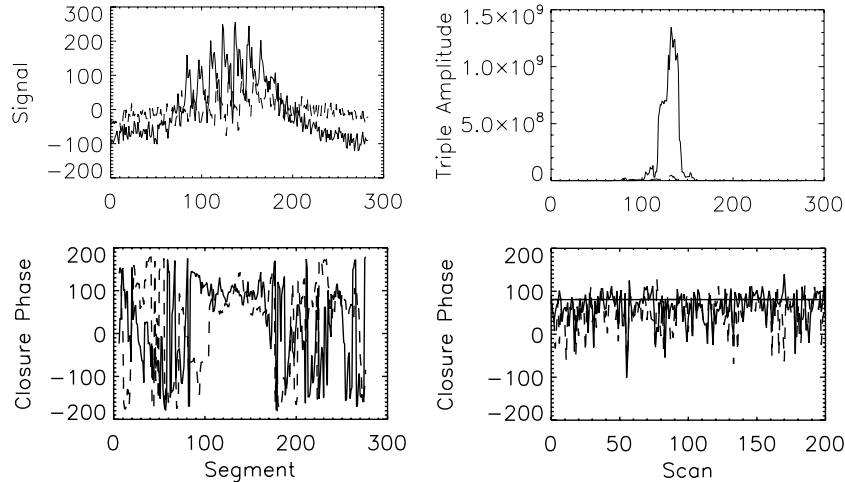
Fig. 9.   Example of extracting the closure phase signal from a single scan. The top left plot shows the raw signals in output pixels B (solid line) and C (dashed line) of a single high SNR scan. The top right plot shows the triple product amplitude of the signals. The bottom left plot shows the closure phase of the two signals, or phase of the triple product. Note how the closure phase is random in the places where the triple product amplitude is zero. The plot at the bottom right shows the triple product amplitude weighted means of the closure phase signals of all scans in the data file.

This calculation can be performed for each segment in each scan in the data set. The final closure phase estimate is produced by first taking the mean of the complex triple product across all scans, and then calculating its phase. This results in a closure phase estimate that is weighted by fringe amplitude.

A last, but very important, consideration is the final sign of the closure phase estimate. All of the calculations described above have been performed with respect to the input beams of the beam combiner, and what we are really interested in is the UV coordinates of the three telescopes projected onto the sky. This calculation is not difficult given the position of the star on the sky and the, assumed

well known, positions of the telescopes on the ground.

4.3.   *Separated fringe packets*

As first noted by Dyck *et al.* (1995b), if one observes a binary star of sufficient separation one will see two separate fringe packets in each scan. An example of this so-called separated fringe packet data (SFP) is given in Fig. 10. The separation of the fringes divided by the projected baseline length is a measurement of the angular separation of the stars in the direction of the baseline projection on the sky. If this measurement is made on several baselines one can obtain the astrometry of the binary star. At the
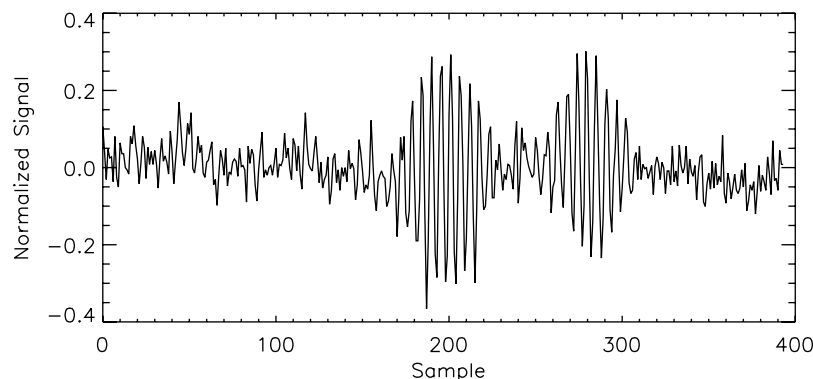

Fig. 10.   Example of separated fringe packet data as used in Farrington *et al.* (2010). This is a single, high SNR, normalized scan taken of the binary star HD 198084 on 2010/09/01.

CHARA Array, the resolution of the SFP technique lies between that of speckle interferometry on large telescopes (for example Mason *et al.* (2012)) and the fitting of visibility amplitudes and closure phases for binary stars whose fringes overlap (for example Li Causi *et al.* (2013)). A particular advantage of the CLIMB beam combiner is that it can obtain three different baselines of SFP data in a very short time since there is no need for a reconfiguration of the array between observations. The SFP technique is explained in detail in Farrington *et al.* (2010).

Another method sometimes employed on SFP data is known as self-calibration. The calibration of interferometric data is only possible by interleaving observations of the primary target with observations of a nearby well known calibrator star. It is sometimes possible to use one object in SFP data as a calibrator, for example on triple stars whose inner pair are unresolved by the SFP technique (O'Brien *et al.*, 2011; ten Brummelaar *et al.*, 2011). This method removes the need for moving between object and calibrator and so can greatly improve observing efficiency.

5. Future Upgrades

An instrument like CLASSIC/CLIMB is never truly finished, and we are continually working to improve its magnitude limit. Two such upgrades

are currently in development — the addition of adaptive optics and a better detector.

5.1. *Adaptive optics*

In 2011 the CHARA Array started a two phased adaptive optics program. Phase I consists of installing wavefront sensors at each telescope, as well as small deformable mirrors in the laboratory. These deformable mirrors will be used to correct for static, or very slow, optical aberrations. Phase II will add the high speed deformable mirrors required at the telescopes to close the AO servo loop. A full closed-loop AO system will not only improve the sensitivity of the Array, but more importantly, it will greatly reduce our sensitivity to changes in seeing. To date, Phase I has been funded by the National Science Foundation and we continue to seek funding for Phase II. Even with just Phase I we expect sensitivity improvements and in particular a large improvement in tip/tilt sensitivity. The AO program is described in much more detail elsewhere in this journal.

5.2. *New HAWAII-1 array detector systems*

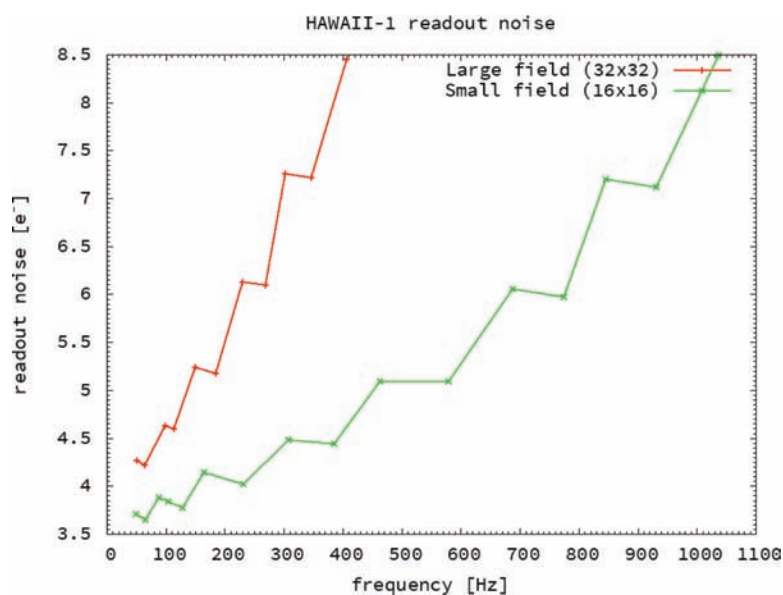As part of a new collaboration with the Max Planck Institute (MPI) for Radio Astronomy, we

Fig. 11. Dependence of the measured read out noise of the HAWAII detector systems on the frame rate for two different sub-window sizes (16×16 and 32×32 pixels). The fastest read out rate in these plots corresponds to 4 ADC samples for each pixel. The steps in this diagram result from the fact that it is not possible to change the number of ADC samples every time the frame rate of the camera is changed. A similar test on a 32×32 area of NIRO gave read out noise of 22.1 as compared to 8.5 for this detector.

are developing two new detector systems for the CLASSIC/CLIMB beam combiner. These detectors are based on the Rockwell HAWAII-1 HgCdTe focal plane array and are expected to have much lower read out noise (see Fig. 11) than the current PICNIC based system. We plan to install the first of these cameras in the summer of 2014 and it will be optimized for a single band, most likely K. The second of these detectors will have more flexibility and several optical filters as well as some spectral resolution. This could be used to provide spectral resolution within each band, or fully separate the bands in order to enable observing simultaneously in more than a single band.

We designed new cold optics, shown in Fig. 12, because the HAWAII-1 FPA has a smaller pixel size (18.5 μm) than the present PICNIC FPA (40 μm). The new cold optics have a point spread function smaller than one pixel over the whole J, H and K′ wavelength range. Presently, CLASSIC/CLIMB observations at different wavelength bands can be made successively only by selecting individual filters in a filter wheel. Therefore, another upgrade goal is to install a non-deviating prism into a filter wheel in the camera in order to image the H- and K-band light onto separate detector pixels and to simultaneously observe in the H and K′ bands.

The new cold optics require more space than those in the existing camera, and so a larger cryostat will be used that also provides the infrastructure and cabling for the HAWAII-1 detector. The detector read out electronics are directly attached to this cryostat. Control communication is done via Ethernet socket connection. The detector data is transmitted via a separate fiber link to an interface board, which then sends the data via a Fire-Wire bus to the data recording computer.

The detector control electronics are built at the MPI for Radio Astronomy. The goal was to achieve the lowest possible read out noise and electronic pick-up noise. The housing of the controller electronics (see Fig. 13) is made from a single block of aluminum within which several chambers have been milled. The individual electronic boards are installed in these separated chambers. The pick-up noise is essentially zero — no pick-up noise peaks
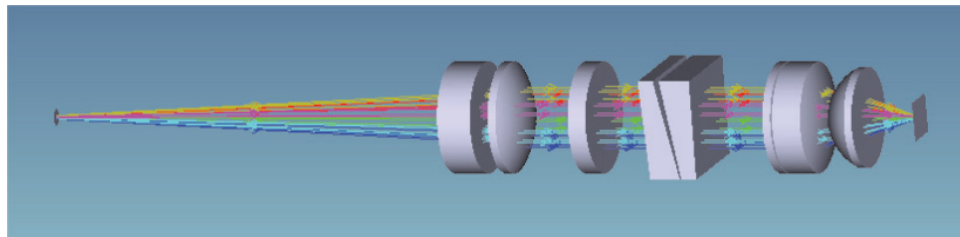

Fig. 12.   Cold optics design for the HAWAII-1 detector. From left to right: focal plane, collimating doublet, filter and non-deviating prism, imaging triplet and detector. The rays represent the six beams of the CLASSIC/CLIMB beam combiner.
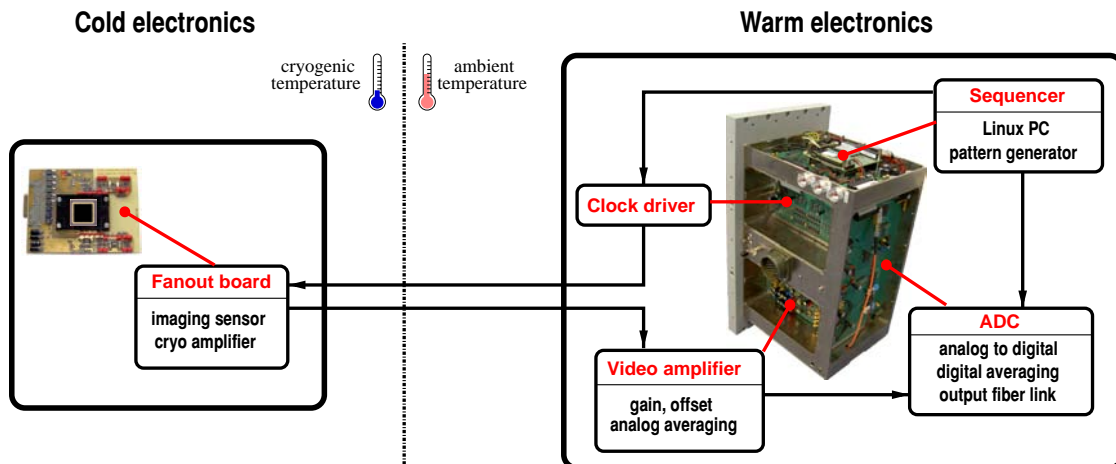

Fig. 13.   Left: detector front-end electronics with the HAWAII-1 FPA on its fan-out board inside the cryostat. Right: controller electronics developed for optimum electronic pickup noise suppression.

are visible in the ensemble-average power spectrum even after thousands of frames. The detector read out noise can be significantly reduced by the following approach: First, the analog detector output signal is processed by a moving boxcar filter consisting of an analog approximation of a finite impulse response filter with a response time adapted to the 10 MHz sample rate of an analog-to-digital converter. Second, a digital filter averages up to 1024 samples for each addressed pixel. This hybrid (analog + digital) filter approach gives a unique flexibility of a programmable bandwidth for optimum noise reduction.

We plan to implement the new detector and optics in two steps: First, we concentrate on K band observations with the highest possible sensitivity and no spectral dispersion. In a second step, the J, H and K′ system including a non-deviating prism will be built. Given the decrease in noise by a factor of 4–5 and an increase in the amount of light by a factor of about 2 when simultaneously observing in several bands, we expect a SNR increase of approximately $\sqrt{2} \times 4.5 \approx 6.4$ or about 2 magnitudes.

5.3. *Multi-band observing capability*

If it were possible to observe in more than one band it would not only increase the UV coverage for each observation but it should be possible to coherently add the fringes in all the bands for use in group delay tracking, thereby further increasing the sensitivity of the system. This could be achieved by adding a dispersive element such that most of the light from each band falls on a different pixel, each separated from the other band by an extra pixel.

The main concern with such a system would be signal to noise loss due to cross talk between the spectral channels. That is, as the seeing gets worse the size of the seeing disk on the camera will become larger and light from one band may reach the pixel for another channel. In order to explore this we extended the simulations discussed in Sec. 2.4.2 to include multiple pixels and spectral dispersion.

Since we have now included dispersion we can no longer perform these simulations for only a single wavelength as we did in Sec. 2.4.2. However, as
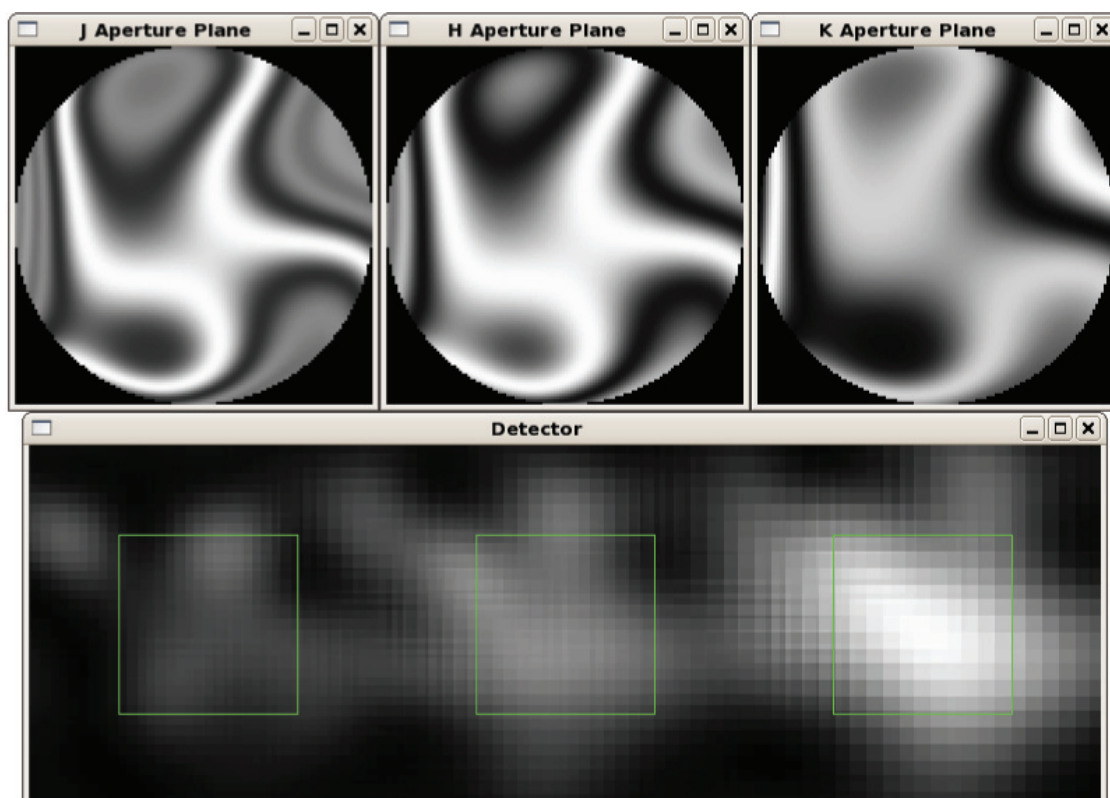

Fig. 14. Example of a single frame of output from modeling multi-band observing. This is for $r_0 = 3\,$cm and a $1\,$ms sample. The squares in the detector plane represent the pixels of interest. Since each band passes through the same turbulent cells the same path-length changes are added to the beam, though since the wavelengths are different this causes different amounts of phase error. The result is the same shape image, but of different sizes.
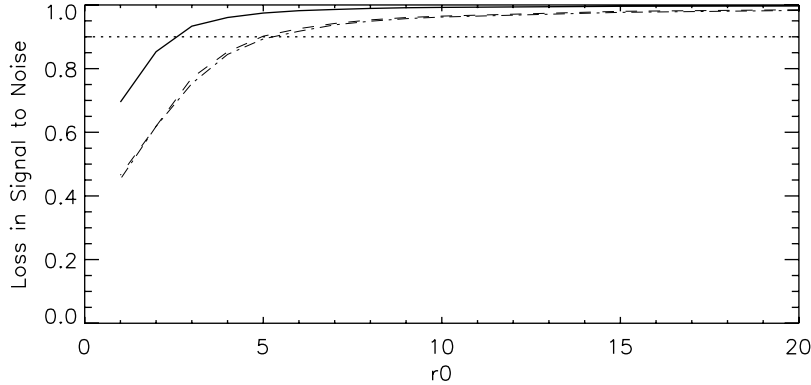
Fig. 15. Plot of the loss of single to noise ratio caused by cross talk of the K′ (solid line), H (dotted line), and J (Dash-dot line) bands.

they take several days to run it was not feasible to perform a full simulation for a large number of wavelengths in each band. For this reason, we have performed the simulation for the three central wavelengths of each band and then used Eq. (7) to calculate the intensity and phase of the electric field across each telescope. Given the phase and amplitude of the electric field for each scope, we can then add these two vectors in order to get the final electric field across the beam splitter whose phase will be

$$\theta = \tan^{-1}\left(\frac{A_1 \sin\theta_1 + A_2 \sin\theta_2}{A_1 \cos\theta_1 + A_2 \cos\theta_2}\right), \qquad (20)$$

and whose amplitude is

$$A = \frac{A_1 \cos\theta_1 + A_2 \cos\theta_2}{\cos\theta}, \qquad (21)$$

where A_i and θ_i are the amplitude and phase of two apertures $i = 1, 2$. The modulus of the Fourier transform will then provide the image as seen on the detector. An example frame of the output of this simulation is given in Fig. 14. One can then calculate the signal to noise ratio of the fringes in each band.

The simulation was run for a range of seeing conditions and for a range of sample times for all three bands at once and for each band individually. We then calculated the loss of signal to noise ratio in each band as a ratio of the SNR in all three bands at once and the SNR of each band individually. We found that the sample time had little effect on this ratio. In reality things will be somewhat worse than these simulations predict as we have made a number of simplifying assumptions. For example there will be more dispersion within each band than

this method takes into account. It is interesting to note that, while you would expect the H band to lie between the J and K′ bands, it has very similar results to the J band. We believe that this is a combination of the different seeing in the three bands, and the fact that the H band pixel contains contamination from both the other bands, while there is only H contamination in the J and K′ bands.

This simulation shows that we do not suffer more than a 10% loss in signal to noise in K′ band until the seeing is worse than approximately 2.5 cm. In practice we have found that in seeing like this our data do not calibrate well in any case. In the J and H bands things are a little worse, where we suffer a 10% loss at $r_0 = 5$ cm. Still, we frequently have seeing much better than this and so we expect that multi-band observing with CLASSIC and CLIMB will be both possible and very advantageous.

6. Conclusion

The CLASSIC/CLIMB beam combiner remains one of our most popular beam combiners and we expect this to continue for some time to come. At the time of writing this paper over a third of the papers published by our group and our collaborators are based on data obtained with CHARA/CLIMB. Some areas of research have been particularly productive, for example oblate fast rotators (McAlister *et al.*, 2005; van Belle *et al.*, 2006; Aufdenberg *et al.*, 2006), Be stars (Gies *et al.*, 2007; Touhami *et al.*, 2013) Exoplanet host stars (Baines *et al.*, 2007, 2008a,b, 2009, 2010b; von Braun *et al.*, 2011a,b; Baines *et al.*, 2011a; von Braun *et al.*, 2012; Baines *et al.*, 2012) the fundamental parameters of a wide range of stellar types (Berger *et al.*, 2006a; Ciardi *et al.*, 2007; Boyajian *et al.*, 2008, 2009; Baines

et al., 2010a, 2011b; Simon & Schaefer, 2011; Boyajian *et al.*, 2012a,b; Baines *et al.*, 2013; Boyajian *et al.*, 2013) and binary and multiple star systems (Bagnuolo *et al.*, 2006; Csizmadia *et al.*, 2009; Farrington *et al.*, 2010; Raghavan *et al.*, 2010; O'Brien *et al.*, 2011; ten Brummelaar *et al.*, 2011; Raghavan *et al.*, 2012). More recently we have obtained the first images based solely on CLIMB data.

CLASSIC/CLIMB has the most sensitivity of all our instruments; indeed we are close to matching the sensitivity of interferometers that have laser guide star AO systems and collecting areas orders of magnitude larger than ours. We plan to continue to find ways to improve the magnitude limit and scientific productivity of this system.

Acknowledgments

References

Aufdenberg, J. P., Mérand, A., Coudé du Foresto, V. *et al.*, 2006, *ApJ*, **645**, 664, doi:10.1086/504149.

Bagnuolo, W. G., Jr., Taylor, S. F., McAlister, H. A. *et al.*, 2006, *AJ*, **131**, 2695, doi:10.1086/501232.

Baines, E. K., Döllinger, M. P., Cusano, F. *et al.*, 2010a, *ApJ*, **710**, 1365, doi:10.1088/0004-637X/710/2/1365.

Baines, E. K., McAlister, H. A., ten Brummelaar, T. A. *et al.*, 2008a, *ApJ*, **682**, 577, doi:10.1086/588653.

Baines, E. K., McAlister, H. A., ten Brummelaar, T. A. *et al.*, 2008b, *ApJ*, **680**, 728, doi:10.1086/588009.

Baines, E. K., McAlister, H. A., ten Brummelaar, T. A. *et al.*, 2009, *ApJ*, **701**, 154, doi:10.1088/0004-637X/ 701/1/154.

Baines, E. K., McAlister, H. A., ten Brummelaar, T. A. *et al.*, 2010b, *AJ*, **140**, 167, doi:10.1088/0004-6256/140/1/167.

Baines, E. K., McAlister, H. A., ten Brummelaar, T. A. *et al.*, 2011a, *ApJ*, **743**, 130, doi:10.1088/0004-637X/743/2/130.

Baines, E. K., McAlister, H. A., ten Brummelaar, T. A. *et al.*, 2011b, *ApJ*, **731**, 132, doi:10.1088/0004-637X/731/2/132.

Baines, E. K., McAlister, H. A., ten Brummelaar, T. A. *et al.*, 2013, *ApJ*, **772**, 16, doi:10.1088/0004-637X/772/1/16.

Baines, E. K., van Belle, G. T., ten Brummelaar, T. A. *et al.*, 2007, *ApJL*, **661**, L195, doi:10.1086/519002.

Baines, E. K., White, R. J., Huber, D. *et al.*, 2012, *ApJ*, **761**, 57, doi:10.1088/0004-637X/761/1/57.

Benson, J. A., Dyck, H. M. & Howell, R. R., 1995, *AO*, **34**, 51, doi:10.1364/AO.34.000051.

Berger, D. H., Gies, D. R., McAlister, H. A. *et al.*, 2006a, *ApJ*, **644**, 475, doi:10.1086/503318.

Berger, D. H., Monnier, J. D., Millan-Gabet, R. *et al.*, 2006b, CHARA Michigan phase-tracker (CHAMP): design and fabrication. In *Society of Photo-Optical Instrumentation Engineers (SPIE) Conference Series*, doi:10.1117/12.672168.

Berger, D. H., ten Brummelaar, T. A., Bagnuolo, W. G., Jr. & McAlister, H. A., 2003, Preliminary results from the longitudinal dispersion compensation system for the CHARA array. In *Society of Photo-Optical Instrumentation Engineers (SPIE) Conference Series*, ed., Traub, W. A., p. 974.

Boyajian, T. S., McAlister, H. A., Baines, E. K. *et al.*, 2008, *ApJ*, **683**, 424, doi:10.1086/589554.

Boyajian, T. S., McAlister, H. A., Cantrell, J. R. *et al.*, 2009, *ApJ*, **691**, 1243, doi:10.1088/0004-637X/691/2/1243.

Boyajian, T. S., McAlister, H. A., van Belle, G. *et al.*, 2012a, *ApJ*, **746**, 101, doi:10.1088/0004-637X/746/1/101.

Boyajian, T. S., von Braun, K., van Belle, G. *et al.*, 2012b, *ApJ*, **757**, 112, doi:10.1088/0004-637X/757/2/112.

Boyajian, T. S., von Braun, K., van Belle, G. *et al.*, 2013, *ApJ*, **771**, 40, doi:10.1088/0004-637X/771/1/40.

Ciardi, D. R., van Belle, G. T., Boden, A. F. *et al.*, 2007, *ApJ*, **659**, 1623, doi:10.1086/512077.

Colavita, M. M., 1999, *PASP* **111**, 111, doi:10.1086/316302.

Colavita, M. M., Boden, A. F., Crawford, S. L. *et al.*, 1998, Keck Interferometer, In *Society of Photo-Optical Instrumentation Engineers (SPIE) Conference Series*, ed., Reasenberg, R. D., p. 776.

Colavita, M. M., Wallace, J. K., Hines, B. E. *et al.*, 1999, *ApJ*, **510**, 505, doi:10.1086/306579.

Csizmadia, S., Borkovits, T., Paragi, Z. *et al.*, 2009, *ApJ*, **705**, 436, doi:10.1088/0004-637X/705/1/436.

Davis, J., Tango, W. J., Booth, A. J. *et al.*, 1999, *MNRAS* **303**, 773, doi:10.1046/j.1365-8711.1999.02269.x.

Dyck, H. M., Benson, J. A., Carleton, N. P. *et al.*, 1995a, *AJ*, **109**, 378, doi:10.1086/117282.

Dyck, H. M., Benson, J. A. & Ridgway, S. T., 1993, *PASP*, **105**, 610, doi:10.1086/133204.

Dyck, H. M., Benson, J. A. & Schloerb, F. P., 1995b, *AJ*, **110**, 1433, doi:10.1086/117617.

Farrington, C. D., ten Brummelaar, T. A., Mason, B. D. *et al.*, 2010, *AJ*, **139**, 2308, doi:10.1088/0004-6256/139/6/2308.

Gies, D. R., Bagnuolo, W. G., Jr., Baines, E. K. *et al.*, 2007, *ApJ*, **654**, 527, doi:10.1086/509144.

Keen, J. W., Buscher, D. F. & Warner, P. J., 2001, *MNRAS*, **326**, 1381, doi:10.1111/j.1365-8711.2001.04718.x.

Li Causi, G., Antoniucci, S., Bono, G. *et al.*, 2013, *A&A*, **549**, A64, doi:10.1051/0004-6361/201220207.

Mason, B. D., Hartkopf, W. I. & Friedman, E. A., 2012, *AJ*, **143**, 124, doi:10.1088/0004-6256/143/5/124.

McAlister, H. A., ten Brummelaar, T. A., Gies, D. R. *et al.*, 2005, *ApJ*, **628**, 439, doi:10.1086/430730.

Millan-Gabet, R., Schloerb, F. P., Traub, W. A. & Carleton, N. P., 1999, *PASP*, **111**, 238, doi:10.1086/316310.

O'Brien, D. P., McAlister, H. A., Raghavan, D., 2011, *ApJ*, **728**, 111, doi:10.1088/0004-637X/728/2/111.

Pedretti, E., Millan-Gabet, R., Monnier, J. D. *et al.*, 2004, *PASP*, **116**, 377, doi:10.1086/383528.

Raghavan, D., Farrington, C. D., ten Brummelaar, T. A. *et al.*, 2012, *ApJ*, **745**, 24, doi:10.1088/0004-637X/745/1/24.

Raghavan, D., McAlister, H. A., Henry, T. J. *et al.*, 2010, *ApJS*, **190**, 1, doi:10.1088/0067-0049/190/1/1.

Sahlmann, J., Ménardi, S., Abuter, R. *et al.*, 2009, *A&A*, **507**, 1739, doi:10.1051/0004-6361/200912271.

Shao, M., Colavita, M. M., Hines, B. E. *et al.*, 1988, *A&A*, **193**, 357.

Simon, M. & Schaefer, G. H., 2011, *ApJ*, **743**, 158, doi:10.1088/0004-637X/743/2/158.

Sturmann, L., Sturmann, J., ten Brummelaar, T. A. & McAlister, H. A., 2010, Modified telescope alignment procedure for improving the beam quality of the CHARA telescopes. In *Society of Photo-Optical Instrumentation Engineers (SPIE) Conference Series*, doi:10.1117/12.857883.

Tango, W. J. & Twiss, R. Q., 1980, *Progress in Optics*, Vol. XVII, p. 241–277, **17**, 241.

ten Brummelaar, T. A., 1995, *Optics Communications*, **115**, 417, doi:10.1016/0030-4018(95)00053-B.

ten Brummelaar, T. A., 1996, *Optics Communications*, **132**, 329, doi:10.1016/0030-4018(96)00407-5.

ten Brummelaar, T. A., McAlister, H. A., Ridgway, S. T. *et al.*, 2005, *ApJ*, **628**, 453, doi:10.1086/430729.

ten Brummelaar, T. A., O'Brien, D. P., Mason, B. D. *et al.*, 2011, *AJ*, **142**, 21, doi:10.1088/0004-6256/142/1/21.

ten Brummelaar, T. A., Sturmann, L., Sturmann, J. *et al.*, 2012, Adaptive optics for the CHARA array. In *Society of Photo-Optical Instrumentation Engineers (SPIE) Conference Series*, doi:10.1117/12.927031.

Touhami, Y., Gies, D. R., Schaefer, G. H. *et al.*, 2013, *ApJ*, **768**, 128, doi:10.1088/0004-637X/768/2/128.

van Belle, G. T., Ciardi, D. R., ten Brummelaar, T. *et al.*, 2006, *ApJ*, **637**, 494, doi:10.1086/498334.

von Braun, K., Boyajian, T. S., Kane, S. R. *et al.*, 2012, *ApJ*, **753**, 171, doi:10.1088/0004-637X/753/2/171.

von Braun, K., Boyajian, T. S., Kane, S. R. *et al.*, 2011a, *ApJL*, **729**, L26, doi:10.1088/2041-8205/729/2/L26.

von Braun, K., Boyajian, T. S., ten Brummelaar, T. A. *et al.*, 2011b, *ApJ*, **740**, 49, doi:10.1088/0004-637X/740/1/49.